Folded Orthotropic Tape-Springs

K A Seffen, B Wang and S D Guest

Department of Engineering, University of Cambridge, Trumpington Street, Cambridge, CB2 1PZ.

kas14@cam.ac.uk, bw407@cam.ac.uk, sdg13@cam.ac.uk

Abstract

We consider the large-displacement, elastic folding of orthotropic tape-springs—thin-walled curved strips made from metal and from a woven laminated composite. Bending of the strips leads to a tight localised fold with a characteristic radius, connected on both sides to straight parts by doubly-curved transition, or *ploy*, regions. We calculate the shapes of these consistent features for a range of orthotropic parameters using geometrically non-linear, compact models. This study is our initial foray into the performance of tape-springs as safety latching mechanisms for aircraft landing gear.

Keywords: tape-springs, composite, orthotropic, folding, large displacements, elastic

1 Introduction

A *composite tape-spring* is, essentially, a carpenter's tape (or tape-measure in the UK) made by laying up flat laminated composite sheets in a cylindrical mould. Conventional heat treatment then follows in order to set its distinctive singly-curved and open shape, Fig. 1(a).

Being thin-walled shells, they can endure significant elastic deformation. They can be compactly rolled along their length for efficient stowage—just like their metal counterparts: their shape is effectively inverted, with the transversely curved width becoming flat and the original axial direction, now uniformly curved to the same degree as the original open curvature, Figs 1(b) and (c).

Unlike metal tape-measures, however, the rolled-up shape can be load-free which, when coupled to the initial shape, results in a *bistable* shell, Fig 1. Bistability can also prevail when the tape is discretely folded away from either end to produce a non-overlapping rolled region connected to mainly straight parts on either side, Fig. 1(d).

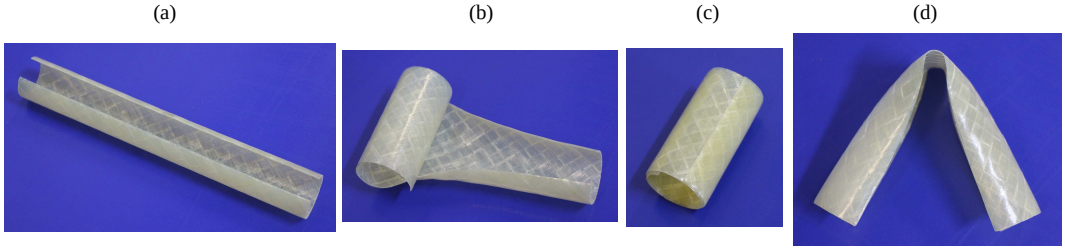

FIGURE 1: Woven laminated composite tape-spring: length 200 mm, transverse radius 12.5 mm, thickness 0.65 mm. (a) Initial extended configuration; (b) partially coiled; (c) fully wound and bistable; (d) folded tape.

The folded tape now behaves as a frictionless hinge, according a free, relative rotation between its ends.

Indeed, it is the absence of holding forces or moments that makes bistability an attractive property for stowage, where the tape will not spontaneously unravel or prematurely straighten.

The factors governing bistable behaviour are a mixture of material constitutive behaviour, initial geometrical proportions, and geometrically non-linear structural behaviour. These have been well documented in, for example [1, 2, 3], where compact but effective conditions for achieving other stable shapes are revealed for orthotropic materials.

We deal with the folded shape of short composite tape-springs proposed for secondary latching structures in aircraft landing gear[1]. Tape-springs are a natural choice because they can be folded at low loads when the gear is retracted and housed, and can straighten during its deployment to prevent accidental retraction of other parts at much higher loads. They are ideally bistable and hence more reliably stowed; at the same time, they must withstand the loading rigours of landing itself. In their design, their folded shape *and* their structural properties must therefore be considered equally.

To focus the breadth of study initially, we consider the folded shape properties, especially the folded radius and the side regions whose length-wise boundary conditions must comply with the fold and the end casings. These so-called *ploy* regions have a natural length scale of minimal deformation, L_{P}, just as the fold has a natural radius of curvature, r, Fig. 2(a.ii).

These lengths, however, may not be able to properly form if the connected tape is too short: it becomes over-confined and liable to damage during folding—whether or not it is bistable, affecting its potential latching operation. Our aim here is to reliably calculate these natural shape properties; for a degree of simplicity, we deliberately *avoid* bistable tapes by choosing appropriate material parameters for a monostable bending response. Continuing study will deal later with the interaction between shape, applied loads and bistability.

In presenting this paper, we align ourselves to Norman Fleck's interests in characterising composite materials [4, 5, 6, 7, 8] and their subservience to the design, performance and capacity of the *structure*, for yielding exciting and novel properties not achieved with traditional engineering materials. We shall not be concerned with Fleckian failure modes although we foresee their relevance; already our tapes can pinch and become damaged during folding if the glass-fibre density is too coarse.

Even though they are much thicker than their metal counterparts, our tapes behave elastically despite large changes in geometry, which speaks again to the remarkable prescience of composites, in general. Our project also showcases a "compliant" application for composites, beyond traditional metrics of maximal stiffness and strength.

In Section 2 we briefly describe how we make our metal and composite tape-springs, and we present their constitutive material behaviour, strain energy densities and bending moment expressions. We then introduce folding experiments in Section 3, where torsional buckling occurs before the tapes "settle" into

[1]See Acknowledgments.

their folded shape. Torsional buckling can be avoided if tapes are bent in their "hard" directions but this produces delamination in composites; it is also more complex to model analytically, with the exception of Mansfield's early work on metallic tapes [9]. Many studies therefore side-step torsional buckling despite its inevitability; we cannot and, thus, begin to study its effect using a simple experimental scheme. We then compare the fully-formed folded radii from finite element analysis to predictions in Section 4: we then assess the ploy shape, first, in dimensional terms in Section 5 before quantifying its length, L_{P}, in Section 6. This study then concludes.

2 Tape-Spring Manufacture and Material Characterisation

Every undeformed tape-spring is characterised by its transverse curvature R, uniform thickness t, subtended angle ξ and length L: the arc-length, b, is $R\xi$, Fig. 2(a.i). Carpenters' tapes can be re-purposed for steel versions ($E = 210$ GPa) by simply cutting a straight length; or thin flat strips of beryllium copper ($E = 131$ GPa) can be age-hardened inside a heated cylindrical former [10]. Typical thicknesses are around 0.1 mm, setting the range for $R/t \approx 50 \sim 200$.

Composite tape-springs are fabricated from "laying-up" three polypropylene sheets with plain-woven reinforcing glass fibres arranged at $\pm 45^\circ$ to the axial and transverse directions. The typical volume fraction of fibres is 30%, and the final thickness is approximately 0.65 mm compared to an initial radius of 12.5 mm.

The lay-up is then wrapped around a cylindrical former and secured using heat-shrink tape over a PTFE-coated glass fabric layer, before placing in a fan-assisted oven at 225°C for four hours. Afterwards, each sample is manually cut to the correct length for testing.

Because the lay-up is effectively symmetrical, there is no evident material coupling between bending and extension, which sets the traditional coupling constitutive matrix, $\mathbf{B}$, to be zero. There is also no local anisotropy *i.e.* no coupling between bending and twisting, nor extension and shearing, which affords the simplest orthotropic description: testing of flat strips then reveals almost identical axial and transverse Young's moduli with a value of 14.5 GPa, a Poisson's ratio of 0.14, and a shear modulus of 0.824 GPa [11].

Following the orthotropic specification in Seffen [12], we also assume plane-stress behaviour, where direct in-plane stresses and strains are denoted as usual by σ and ϵ. A single subscript indicates the coordinate (x, y) direction, with x aligned length-wise and y transverse, always.

E_x and E_y are the orthogonal Young's moduli in ratio β: even though our composite tapes exhibit roughly the same values, we can examine in theory, at least, the effects of a modular difference. The corresponding Poisson's ratios are ν_{xy} and ν_{yx}, which are correlated from the Reciprocal Theorem by $\nu_{xy}/E_x = \nu_{yx}/E_y$. Defining other constants for brevity, the complete specification is written:

$$E_x = E, \quad E_y = \beta E, \quad G = \rho E, \quad \nu_{yx} = \nu, \quad \nu_{xy} = \frac{\nu}{\beta} \tag{1}$$

The shear modulus is G with $\rho = 1/2(1+\nu)$ for isotropic behaviour ($\beta = 1$). An homogenous material response through the thickness is fairly assumed for thin laminates, with in-plane orthogonal strains now given by:

$$\epsilon_x = \frac{\sigma_x}{E} - \frac{\nu\sigma_y}{\beta E}, \quad \epsilon_y = -\frac{\nu\sigma_x}{\beta E} + \frac{\sigma_y}{\beta E}, \quad \gamma_{xy} = \frac{\tau_{xy}}{\rho E} \tag{2}$$

along with γ_{xy} and τ_{xy}, the shear strain and its stress. The above can be inverted to give explicit stresses, $\sigma_x = E \cdot (\epsilon_x + \nu\epsilon_y)/(1-\nu^2/\beta)$ *etc.*, if desired.

Bending and stretching of any tape-spring is expressed by the deformation of its internal middle surface. When in-plane behaviour correlates to the above stresses and strains, the corresponding stretching strain energy density per unit surface area can be written as:

$$U_{\mathrm{S}} = \frac{t}{2} \cdot [\sigma_x\epsilon_x + \sigma_y\epsilon_y + \tau_{xy}\gamma_{xy}] = \frac{t}{2E} \cdot \left[\sigma_x^2 + \frac{\sigma_y^2}{\beta} - \frac{2\nu\sigma_x\sigma_y}{\beta} + \frac{\tau_{xy}^2}{\rho}\right] \tag{3}$$

When there are changes in curvature of the middle surface, χ_x and χ_y, and any change in twisting curvature, χ_{xy}, the strains vary linearly with material height z through the thickness from Kirchoff's hypothesis [13], setting $\epsilon_x = z\chi_x$, $\epsilon_y = z\chi_y$ and $\gamma_{xy} = 2z\chi_{xy}$. We take χ_{xy} to be the *engineering* version of twist, and χ generally expresses the difference between the *current* curvature, κ, and any initial, stress-free value, κ_0, thus $\chi = \kappa - \kappa_0$.

Bending moment stress resultants follow with $M_x = \int \sigma_x \mathrm{d}z$, and so forth, through the thickness (and per unit in-plane length), to yield the set of generalised Hooke's laws for orthotropic bending:

$$M_x = \frac{Et^3}{12(1-\nu^2/\beta)} \cdot [\chi_x + \nu\chi_y], \quad M_y = \frac{Et^3}{12(1-\nu^2/\beta)} \cdot \left[\chi_y + \frac{\nu\chi_x}{\beta}\right], \quad M_{xy} = \frac{Et^3\rho}{6}\chi_{xy} \tag{4}$$

The corresponding strain energy density in bending is equal to $(1/2) \cdot (M_x\chi_x + M_y\chi_y + 2M_{xy}\chi_{xy})$, *i.e.*

$$U_{\mathrm{B}} = \frac{D}{2} \cdot \left[\chi_x^2 + \beta\chi_y^2 + 2\nu\chi_x\chi_y + 2\alpha\chi_{xy}^2\right] \tag{5}$$

with D as the flexural rigidity, $Et^3/12(1-\nu^2/\beta)$, and α as the dimensionless torsional rigidity, $4(1-\nu^2/\beta)\rho$, equal to $(1-\nu)$ for isotropic materials. For our composite tapes specifically, $\alpha \approx 0.11$.

3 Folding Experiments

When a tape-spring is bent uniformly by equal and opposite end moments, M, the curved cross-section *flattens* before eventually localising into a fold of constant radius, r, over an axial length equal to $2r\theta$. On either side the fold is connected to virtually straight parts by initial ploy regions which re-acquire the original transverse curvature over a length L_{P}, Fig. 2(a.ii).

When r and R lie on same surface side of the tape, we have so-called *equal-sense* bending [14], Fig. 2(b.i), and *vice versa* for opposite-sense bending, Fig. 2(b.ii). Using the commercial finite element analysis (FEA) software package ABAQUS [15], we can simulate a typical moment-rotation response, shown in Fig. 2(c) for a metal tape made of four-noded, reduced integration thin-shell elements. Geometrically non-linear large displacements are enabled, and the solution scheme uses a default stabilisation protocol to enable convergence.

M is linear initially in both directions but quickly succumbs to either flattening and snapping (opposite sense, $M > 0$) or to softer torsional buckling (equal sense, $M < 0$). Around end rotations of 0.3 and 0.5 radians (17° and 29°), respectively, the moments reach similar, steady values M_*^+ and M_*^- as the folds become established. Even though θ increases, the moments remain constant as the fold region "grows" in length.

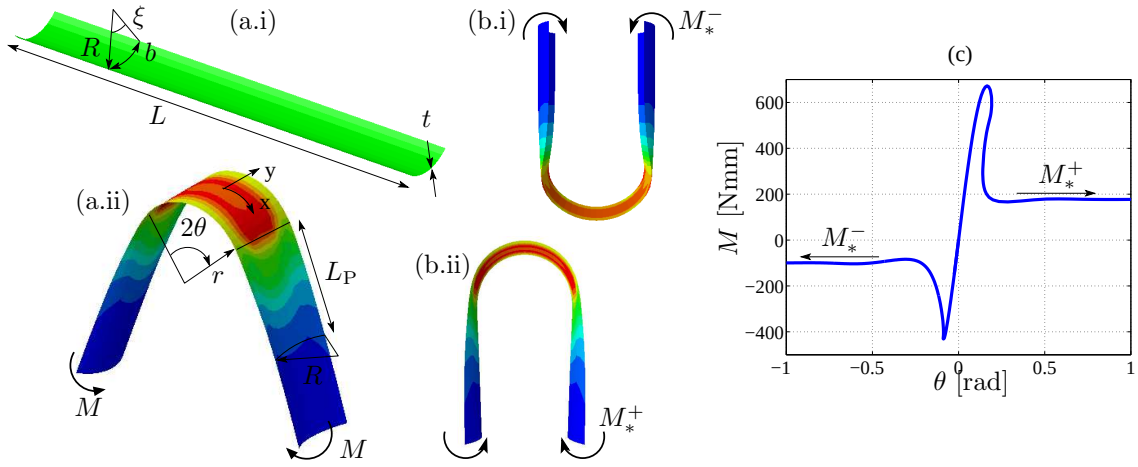

FIGURE 2: (a.i) Tape-spring geometry via R, t, L, ξ, and b ($= R\xi$); (a.ii) uniformly folded tape-spring via finite element analysis (FEA): fold radius is r and subtends angle 2θ, and the transitional ploy region extends from each fold end by L_P to practically undeformed parts; contours are Mises stresses. (b.i) Equal- and (b.ii) opposite-sense folding with constant end moments, M_*^- and M_*^+. (c) Typical FEA moment-rotation (M, θ) response for $R = 10$ mm, $t = 0.2$ mm, $L = 100$ mm and $\xi = 90°$ (isotropic material).

Performing a similar practical experiment necessitates a bespoke and, hence, expensive bending rig, able to apply precise uniform bending moments and end rotations [10]. Because the ends must be securely held, the scope for torsional buckling during equal-sense bending, manifestly apparent during manual bending of a lengthy tape, is clearly reduced.

We pursue instead a simpler *three-point* bending arrangement, shown schematically in Fig. 3(a). Miniature holes are drilled into a horizontal tape at collinear points A, B and C, very close to the ends and in the middle, in order to secure long vertical wires. The outer two are anchored downwards, and the middle one pulls upwards to generate a force, F, and mid-point displacement, δ, Fig. 3(a.iii).

Because the ends are free to twist and rotate, torsional deformation during equal-sense bending is unimpeded, Fig. 3(b.i). When the same tape geometry and boundary conditions are simulated in the FEA, there

is a remarkable one-to-one correspondence in deformed shape, Fig. 3(b.ii); note that the tape is not perfectly circular throughout but has flat flanks, Fig. 3(a.ii).

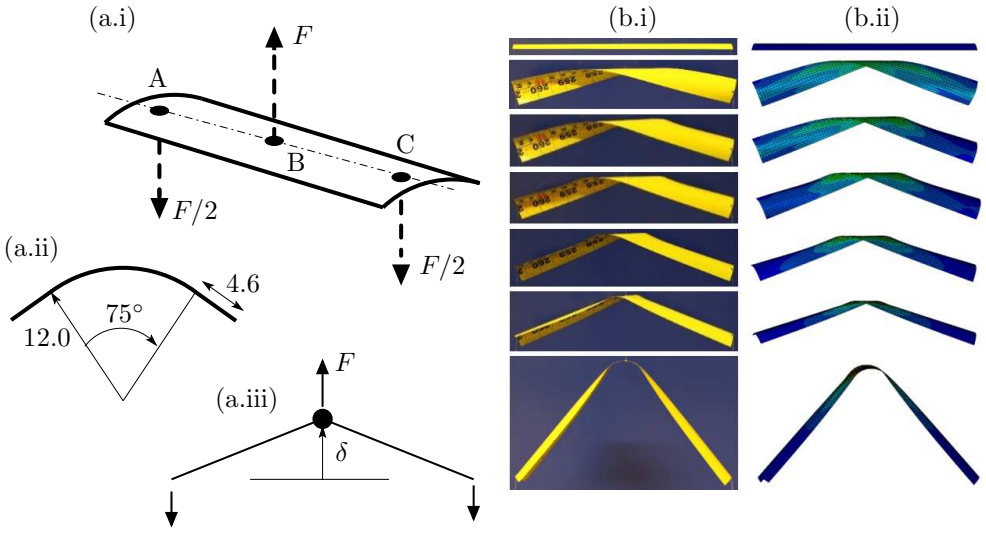

FIGURE 3: (a.i) Schematic three-point bending test for tape-spring: collinear and central wire attachment points, A, B and C; (a.ii) cross-sectional geometry [mm] of steel carpenter's tape; (a.iii) measured force, F, and vertical displacement, δ, at centre-point. (b.i) Typical coupled equal-sense bending and twisting deformation; (b.ii) matching FEA simulations, where contours are Mises stresses.

Formal measurements for a composite tape-spring of length 200 mm and subtended angle $\xi = 180°$ ($R = 12.5$ mm, $t = 0.65$ mm from Section 2) are indicated in Fig. 4. There are four clear stages of robustly repeatable deformation, which are observed also for metal tapes, and highlighted schematically. Stage I is initial, symmetrical equal-sense bending followed by buckling at $F = F_{\text{crit}}$ into a global torsional mode at the onset of stage II, with a drop in stiffness *viz.* gradient. During stage III, deformation begins to localise centrally with increased curving at the expense of twisting and a declining force; by stage IV, the untwisted fold has fully formed and the force increases again. Note that because F is non-zero throughout deformation, the tape cannot be bistable.

Finite element analysis also reveals the same traits, where the composite is simulated at the level of individual plies using Naik's model [16]: their woven nature is captured by one isotropic "matrix" layer and two uni-directional laminates for each $\pm 45°$ direction, all constructed with the same S4R elements as per metal tapes. Geometrical non-linearity is also permitted, and a damping factor of 1×10^{-6} is specified for stabilisation. Preliminary convergence studies have shown that an element edge length no more than 1% of the tape length is sufficient for accuracy.

The black curve retains the movement of supports A, B and C, Fig. 2(a.i), in a vertical plane, which converges straightforwardly. In reality, these points move in and out of plane to yield the grey curve, where convergence has to be more stringently enforced. The grey curve better follows the earlier stages, in particular the size of the peak moment, F_{max}, and the latter variations of both curves approximate well the

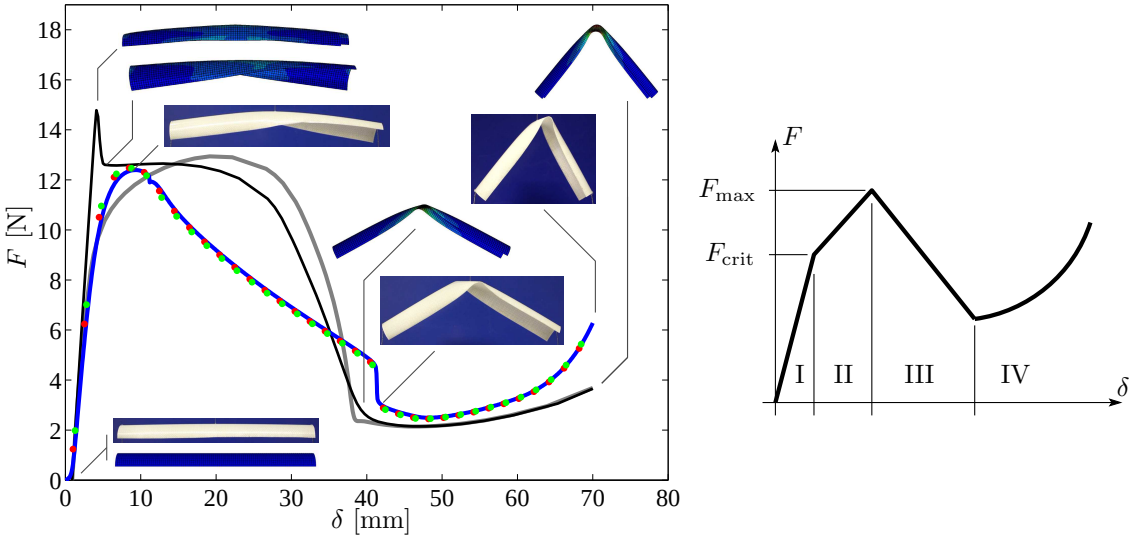

FIGURE 4: Force-displacement curves from three-point equal-sense bending of composite tape, with $R = 12.5$ mm, $t = 0.65$ mm, $L = 200$ mm and $\xi = 180°$. Left, blue curve is experimental test, repeated twice (red/green dots): grey curve is FEA for wire supports able to move out of plane in Fig. 3(a.i) and black curve has supports always coplanar. Right, schematic (F, δ) response: (I) linear bending, (II) torsional buckling, (III) localisation, (IV) folding.

experimental response of the nascent fold.

The overlapping region of stages II and III is however discrepant, with the experimental force diminishing more quickly after buckling commences. Although difficult to see from the inset figures, the buckling mode produces "pinching" of the free edges in practice rather than the locally smooth distortion seen in the FEA. Pinching seems to arise from local buckling or compressive damage of the matrix between fibres along the free edge. Even though it initiates because of torsional buckling, the response of the softer matrix then controls the post-buckling behaviour by lowering the applied forces prematurely, we surmise.

The inset figure also shows a rotated fold axis during stage IV, which diminishes for large fold angles but not altogether. Again, pinching causes some of the earlier twist to become "locked in" to the folded shape, which is clearly different from the FEA fold, which quickly loses its initial rotation. Note that opposite-sense bending is amenable to the same experimental scheme, where a snap-though response follows the peak moment for metal tapes; the much larger subtended angle of our composite tapes precludes a similar undamaged response.

The equal-sense performances have encouragingly similar features but there also notable differences during stages II and III that require additional study. The formation of a fold and ploy regions is evident but in order to study the properties of a "well-developed" and uniform fold, we revert to uniform tape bending using FEA in the following section.

4 Large Displacement Folding

Figure 5 shows four folded tapes with different orthotropic modular ratios, β, but all with the same E, ν, and G, and radius $R = 10$ mm, subtended angle $\xi = 90°$, and thickness $t = 0.2$ mm. Each has been uniformly bent, *c.f.* Fig. 2(b), in order to establish uniform r throughout the fold region, as shown; opposite-sense bending is preferred only because the fold becomes well-developed much earlier; as we shall see, its radius does not depend on the direction of bending.

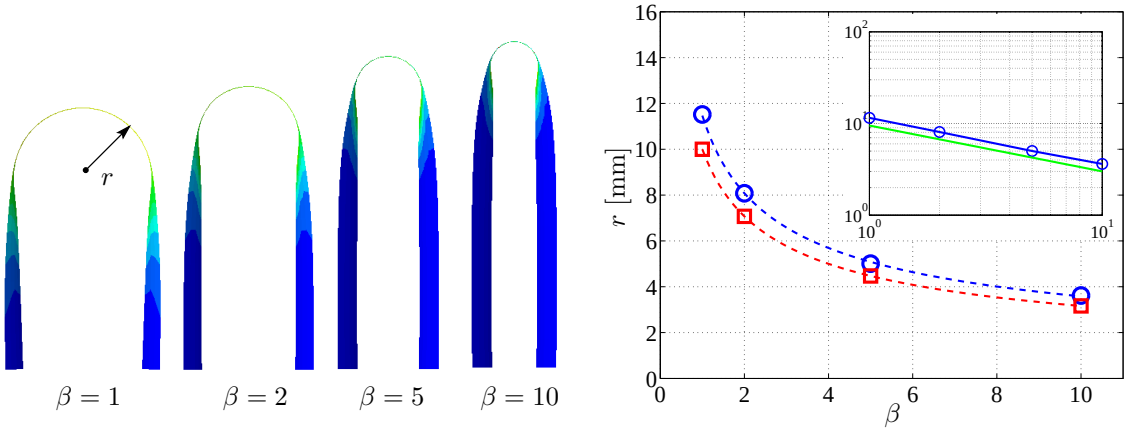

FIGURE 5: Uniform opposite-sense folded tapes from FEA where contours are Mises stresses. Right, measured fold radii, r (blue) *vs* predictions (red). Inset: power-law fit for measured values (blue) equal to $11.47\beta^{-0.51}$, which is plotted dashed (blue) in main figure; the green line has a slope of -1/2 for comparison. $R = 10$ mm, $\xi = 90°$, $t = 0.2$ mm, $E = 131$ GPa, $\nu = 0.3$, $\alpha = 1 - \nu$ for all tapes.

The data are almost exactly fitted by the curve $11.47\beta^{-0.5051}$, with an exact index of $-1/2$ being assured. Given that no other parameters are varied, the data are consistently 14.7% larger than R. In the isotropic case, $\beta = 1$, the fold radius is often cited as being equal to R but an early study reported a regular difference up to 15% from other simulations [17]. It would seem the same disparity applies for orthotropic tapes, which is being studied further.

The axial curvature of a uniformly bent fold appears to depend on $\beta^{1/2}$, amongst other things, but not the relative rotation between the ends of tape: the same tightening of radius is observed, somewhat informally, in the latter stages of our three-point bending tests.

For uniform bending, it is usual to assume that any changes in strain energy in a folded tape-spring are due to the fold alone and not to the ploy regions, which maintain a fixed shape. Because the shape of fold has changed from one type of open cylinder to another, there is only *developable* bending deformation and negligible stretching [18]. The developable assumption coupled to uniform curvatures also allows us to treat tapes with large subtended angles as being shallow shells in view of the strain energy stored, Eqn 5, because it is written in terms of curvature changes.

The specific change in axial curvature, χ_x, is $1/r$, there is no twisting curvature, and $\chi_y = \pm 1/R$, where R is the original transverse radius of curvature: the $\pm$ sign accords opposite/equal-sense bending, respectively.

The total strain energy in bending, $\bar{U}_{\mathrm{B}}$, multiplies the energy density, Eqn 5, by the surface area of fold:

$$\bar{U}_{\mathrm{B}} = 2r\theta b \cdot \frac{D}{2}\left[\chi_x^2 + \beta\chi_y^2 + 2\nu\chi_x\chi_y\right] = Db\theta\left[\frac{1}{r} + \frac{\beta r}{R^2} \mp \frac{2\nu}{R}\right] \tag{6}$$

A minimal energy configuration sets $\partial\bar{U}_{\mathrm{B}}/\partial r$ equal to zero, which returns $r = R/\sqrt{\beta}$ for bending in both directions. The index of one-half is confirmed and the expression for r matches that first postulated in [19], then in [20] for carbon-fibre reinforced plastic (CFRP) tapes, with both written using different notation.

This expression may also be used to validate the axial bending moment required to sustain the folded shape, $M_*^{\pm}$, using the expressions from Eqn 4. Multiplying them by the flattened width b expresses the total moment:

$$M_*^{\pm} = \frac{b}{R} \cdot \frac{Et^3}{12(1-\nu^2/\beta)}\left[\sqrt{\beta} \pm \nu\right] \tag{7}$$

after substituting for χ_x and χ_y: the same expression is returned by differentiating $\bar{U}$ with respect to θ.

M_*^+ values from Eqn 7 are superposed onto the (M, θ) curves from the FEA in Fig. 6 over the same rotation range. The correlation is very good throughout with Eqn 7 being no more than 10% larger on closer inspection: the size of this discrepancy would seem to fit with the differences expressed between the radii predictions in Fig. 5, and is also recorded in [20] for their CFRP tapes. Note that we would also expect $M_*^{\pm}$ to increase linearly with subtended angle, given the proportional relationship to b in Eqn 7; but since r does not appear to depend on ξ, we do not formally confirm this expectation.

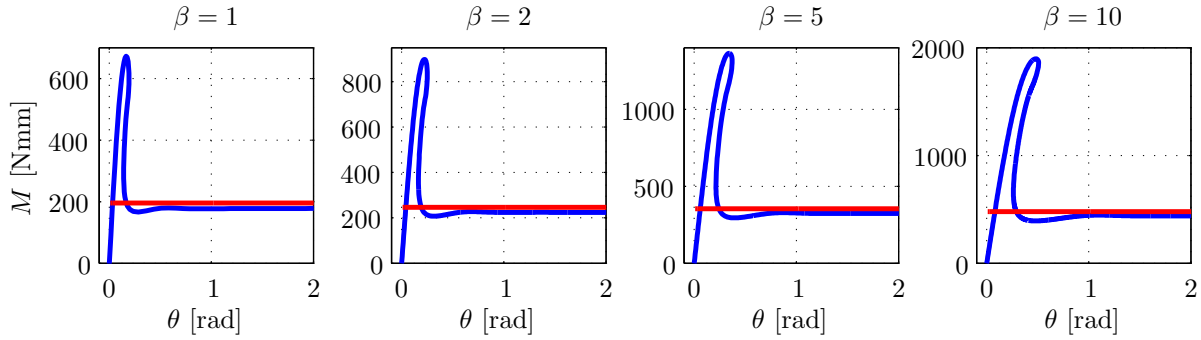

FIGURE 6: Opposite-sense orthotropic moment-rotation response from FEA for the same tapes from Fig. 5. Red lines are constant M_*^+ predictions from Eqn 7.

5 Ploy Shape: Dimensional Expectations

The ploy regions extend for a length many times larger than the thickness t and on the scale of the original transverse radius of curvature R. Such behaviour is purported to be a *long-wave* solution within the classical Donnell equations for deformation of an initially cylindrical shell [13]. The pair of variables in that case are

the radial displacement, w, and the Airy Stress function, ϕ, tantamount to in-plane forces, which both vary in the x (axial) and y (circumferential) directions.

The cylindrical nature assumes a closed shell but our open cylindrical tape is governed equivalently provided we reflect the same boundary conditions along its edges—as if having excised a strip from the original closed shell with no edge loading. The w and ϕ functions adopted in [13] both multiply an eigenfunction, $\sin(\pi y/b)$, by separate x-wise variations before being submitted to Donnell's equations: our strip conforms exactly to the required edge conditions if it has a transverse arc-length of b.

The long-wave solution is dominated by axial stretching and circumferential bending, which allows us to "switch off" certain parts within the Donnell set, as carefully laid out in [13]. The resulting pair of coupled differential equations in w and ϕ are simplified approximations of geometrical compatibility and equilibrium for bending and stretching together; similar forms have been obtained elsewhere, for example, when describing the "persistence" of end-wise pinching of an isotropic pipe [21].

If we repeat the long-wave derivation in [13], however substituting for our orthotropic material laws, we ultimately arrive at the equivalent pair of governing second-order differential equations:

$$\frac{\pi^4}{b^4}\cdot\phi - \frac{E}{R}\frac{\mathrm{d}^2 w}{\mathrm{d}x^2} = 0, \quad D\beta\frac{\pi^4}{b^4}\cdot w + \frac{t}{R}\frac{\mathrm{d}^2\phi}{\mathrm{d}x^2} = 0 \tag{8}$$

These differ from Donnell's original in two ways. The modular ratio, β, is now present; our ϕ is a stress function, differing from ϕ in [13], a force function, by a factor of thickness, t, which makes no difference to the outcome shortly.

Substituting ϕ from the first equation into the second, and differentiating twice with respect to x, produces a fourth-order equation in w alone:

$$\frac{\mathrm{d}^4 w}{\mathrm{d}x^4} + \frac{DR^2\beta\pi^8}{Etb^8}\cdot w = 0 \tag{9}$$

Writing the pre-factor of w as $4k^4$, we can establish a characteristic length scale, l, equal to π/k, from the general solution. Equating terms and re-arranging in terms of l, we arrive at:

$$l = \frac{b^2}{\pi R^{1/2}}\left[\frac{4Et}{D\beta}\right]^{1/4} \quad \rightarrow \quad l = \frac{2}{\pi}\cdot\left[\frac{3(1-\nu^2/\beta)}{\beta}\right]^{1/4}\cdot\frac{b^2}{R^{1/2}t^{1/2}} \tag{10}$$

The particular boundary conditions at both ends of the ploy region ultimately dictate the numerical scale of this expression, making $2\cdot 3^{1/4}\ldots/\pi$ irrelevant for now. If $\beta >> \nu^2$, the essential dimensional variation of l goes with $b^2\cdot R^{-1/2}\cdot t^{-1/2}\cdot\beta^{-1/4}$. For a fixed width and material, $l \sim 1/\sqrt{Rt}$, which is precisely the inverse relationship observed when dealing with "short-wave" solutions *i.e.* boundary layer effects of Donnell's equations. We can of course shorten the expression by writing b as a proportion of R, setting $l \sim R^{3/2}\cdot t^{-1/2}\cdot\beta^{-1/4}$, as in [21], giving fewer parameters to vary when characterising l experimentally.

This long-wave approach is essentially a leading-order solution, now being deployed more frequently in highly-deformable plates and shells problems, and doubtless inspired by the "French" school of thought; for example see [22, 23]. As noted, circumferential bending and axial stretching are pre-eminent physical effects in Donnell's equations, expressed by the highest variations in w and ϕ.

Equivalently, the axial variation of the y-wise curvature "leads", compared to the changes in the x-wise curvature or in the twisting curvature; as do the axial strains compared to the rest. Switching to a lower order kinematical variable such as curvature (compared to w) permits some reductions in complexity of solution if we adopt instead a strain energy formulation; and in turn, enables us to quantify the boundary conditions more simply, for a corresponding ploy length (approaching these from a stress resultant viewpoint is certainly more involved: see [13].)

6 Ploy Shape: Size

The numerical pre-factor in Eqn 10 has a value close to unity, around 0.8 for $\nu = 0.3$ and $\beta = 1$. From finite element simulations shown momentarily, this tends to overshoots by some way. As ever, assuming that certain kinematic terms are dominant in Donnell's equations subtracts from the general application of the long-wave result; that the ploy length is somewhere between long and short.

A more general and direct analysis was originally produced by Jain and Rimrott in 1971 on the closely related subject of STEMS—Storable Tubular Extendable Members [24] . These are metal tape-spring slit tubes enveloping nearly 2π radians of cross-section, capable of being wound onto a drum and then deployed on a spacecraft for gravity compensation, instrument positioning *etc.*

From the outset, they deal with changes of curvatures, χ, in the ploy region, assuming that one end has been completely flattened, the other being fully rounded and unstressed, see Fig. 7. Transverse moment equilibrium is simplified crucially by assuming that the double rate of change of transverse curvature along the STEM, $\partial^2\chi_y/\partial x^2$ dominates, as per Donnell; but that the equivalent rate for the change in curvature along, $\partial^2\chi_x/\partial x^2$, is some fixed proportion, a, of the principal rate.

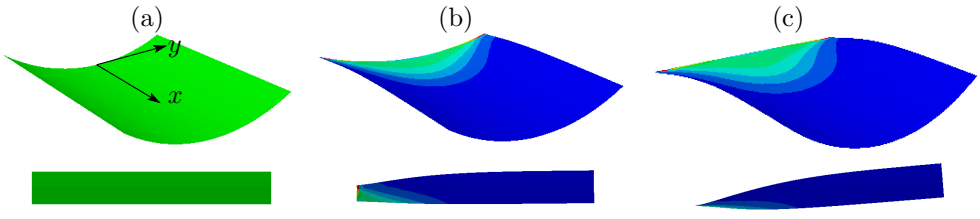

FIGURE 7: Ploy length assessment via FEA. (a) Initial geometry; (b) intermediate flattening of far-field edge; (c) edge flattened. Contours are Mises stresses, and bottom views are in elevation. Geometry: $R = 10$ mm, $t = 0.2$ mm and $\xi = 60°$. The modular ratio, β, is equal to ten, in order to highlight a more rapid decay compared to an isotropic tape.

Employing the Codazzi-Mainardi compatibility equations, they arrive at a final governing equation for

χ_y:

$$\frac{\partial^2 \chi_y}{\partial x^2} + k^2 \frac{\partial^2 \chi_y}{\partial y^2} = 0 \tag{11}$$

where $k = \sqrt{1+a}$ and ultimately is a decay parameter.

Jain and Rimrott employ a Fourier series solution for χ_y, which sums to a uniform $-1/R$ at the flat end, and to zero at x equal to "infinity", for simplicity: only opposite sense flattening is dealt with but the result can be extended easily for $\chi_y = +1/R$ at $x = 0$. They are then able to find the corresponding changes in transverse curvature, χ_x, and twisting curvature, χ_{xy}.

If instead we take a leading order solution for χ_y, equal to $f(x)\cos(\pi y/b)$ and substitute into Eqn 11, then

$$\frac{\mathrm{d}^2 f}{\mathrm{d}x^2} - \frac{k^2\pi^2}{b^2} f = 0 \quad \rightarrow \quad \chi_y = -\frac{1}{R} \cdot \exp\left(-k\pi x/b\right) \cos\left(\pi y/b\right) \tag{12}$$

which complies with the earlier boundary conditions. The other changes in curvature follow from the Codazzi-Mainardi equations again, with

$$\chi_{xy} = \frac{k}{R} \cdot \exp\left(-k\pi x/b\right) \sin\left(\pi y/b\right), \quad \chi_x = -\frac{k^2}{R} \cdot \exp\left(-k\pi x/b\right) \left[1 - \cos\left(\pi y/b\right)\right] \tag{13}$$

Jain and Rimrott acknowledge that because the bending solution foists a change in Gaussian curvature, there is also in-plane stretching primarily along the ploy length—again, in the same direction in Donnell's cylinders.

The expression for the former in terms of curvature changes (rather than absolute terms, Eqn **??**) is shown to be $-\chi_{xy}^2 + \chi_x\chi_y + \chi_x/R$ in [24]. Considering Eqns 12 and 13, the order in size of contributions from all changes in curvature are the same, and all must be included in the relationship to $\partial^2\epsilon_x/\partial y^2$. We may therefore write, substitute and calculate:

$$\frac{\partial^2 \epsilon}{\partial y^2} = \chi_{xy}^2 - \chi_x\chi_y - \frac{\chi_x}{R} = \frac{k^2}{R^2} \cdot \left[\exp\left(-k\pi x/b\right) + \exp\left(-2k\pi x/b\right)\right] \cdot \left[1 - \cos\left(\pi y/b\right)\right] \tag{14}$$

This expression is then integrated twice with respect to y to give the strain and thence axial stress. The constants of integration follow from setting the nett axial force to be zero *i.e.* $\int \epsilon_x \mathrm{d}y = 0$ between limits of $\pm b/2$. For our solution, it can be shown:

$$\epsilon_x = \frac{k^2}{R^2} \cdot \left[\exp\left(-k\pi x/b\right) + \exp\left(-2k\pi x/b\right)\right] \cdot \left[\frac{y^2}{2} + \frac{b^2}{\pi} \cdot \cos\left(\pi y/b\right) - \frac{b^2}{24} + \frac{2b^2}{\pi^3}\right] \tag{15}$$

To find k, the usual strain energy components from bending and stretching are assembled. In the case of bending, Eqn 5, the dominant product term is χ_y^2, which varies with $1/R^2$; for the others, $(\chi_{xy}^2, \chi_x\chi_y) \sim$

k^2/R^2 and $\chi_x^2 \sim k^4/R^2$, which are much smaller because k is usually less than unity. The final total energy expression is thus:

$$\bar{U} = \bar{U}_\mathrm{B} + \bar{U}_\mathrm{S} = \int\int U_\mathrm{B} + U_\mathrm{S}\ \mathrm{d}x\mathrm{d}y = \int_{-b/2}^{+b/2}\int_0^{\inf} \frac{1}{2}\left[D\beta\chi_y^2 + Et\epsilon_x^2\right]\ \mathrm{d}x\mathrm{d}y \tag{16}$$

Substituting for χ_y and ϵ_x, and performing the integration, we arrive at:

$$\bar{U}_\mathrm{B} = B \cdot \frac{D\beta b^2}{R^2 k}, \quad \bar{U}_\mathrm{S} = S \cdot \frac{Etb^6k^3}{R^4} \tag{17}$$

where B is a constant equal to $1/8\pi \approx 0.039$, and $S = 9.18 \times 10^{-6}$. The proper value of k minimises $\bar{U}$ by differentiating with respect to k and setting equal to zero, *i.e.*

$$k^4 = \frac{B}{3S} \cdot \frac{D\beta}{E} \cdot \frac{R^2}{tb^4} \quad \rightarrow \quad k^4 = \frac{B}{36S} \cdot \frac{\beta}{1-\nu^2/\beta} \cdot \frac{t^2R^2}{b^4} \tag{18}$$

Returning to Eqn 12, the characteristic length of decay and thus ploy length, denoted now as L_P in accordance with Fig. 2(a.ii), is set by the index of the exponent. To compare directly with Donnell's solution, Eqn 10, we set $L_\mathrm{P} = b/\pi k$ to give:

$$L_\mathrm{P} = \left[\frac{1-\nu^2/\beta}{\beta} \cdot \frac{36S}{\pi^4 B}\right]^{1/4} \frac{b^2}{R^{1/2}t^{1/2}} \tag{19}$$

For $\nu = 0.3$ and $\beta = 1$, the numerical pre-factor is around 0.093: this is considerably smaller than the prediction from Eqn 10 because all curvature terms now contribute to the level of Gaussian curvature.

But it seems self-defeating to declare a specific ploy length in view of the decaying nature of the problem; an index equal to -1 lends a reduction in parameter values of only 63%. We can, of course, compare different predictions of L_P for the same measure, but it is better to compare the decaying *variation* due to k originally. Comfortingly, there is the same long-wave dependency of L_P on $b^2 \cdot R^{-1/2} \cdot t^{-1/2} \cdot \beta^{-1/4}$ as in l from Donnell.

We shall see that our decay profiles tend to fit simulations generally better but are not always accurate. If this is due to employing a single leading-order term for each of our curvature changes, we can reconsider the Fourier series solution for χ_y given by Jain and Rimrott [24]:

$$\chi_y = -\sum_{n=1,3,5\ldots}^{\inf} \frac{4}{n\pi R} \cdot (-1)^{(n-1)/2} \cdot \exp\left(-kn\pi x/b\right) \cdot \cos\left(n\pi y/b\right) \tag{20}$$

with the other curvatures being similarly expressed.

Although the change in Gaussian curvature and bending strain energy can be found in closed form despite the infinite sum, ϵ_x and the stretching component of U cannot—requiring numerical integration for a very large number of n terms towards finding k. Because we wish to include the effects of the orthotropic parameter, β, we are obliged to do the same.

No matter the number of terms, n, taken for χ_y *etc.*, $\bar{U}_\mathrm{B}$ and $\bar{U}_\mathrm{S}$ can always be expressed in the same dimensional form of Eqns 17: this point is missed for $\bar{U}_\mathrm{S}$ in [24], which is returned as a curve for certain choices of physical properties.

We therefore evaluate the integrations for $\bar{U}$ symbolically using MATLAB [25] for n increasing, in order to extract the pre-factors B and S. Consequently: $(B,S) = (0.0645, 1.842 \times 10^{-5})$ for $n = 1$, $(B,S) = (0.0669, 8.2657 \times 10^{-6})$ for $n = 3$ and $(B,S) = (0.0674, 8.053 \times 10^{-6})$ for $n = 5$. For higher values of n, the evaluations fail to converge owing to the sheer length of expressions.

Notwithstanding, the values of B and S appear to quickly settle to steady values, with their ratio, B/S, moving from our very first value of $0.039/9.18 \times 10^{-6} = 4336$ to around $0.0674/8.053 \times 10^{-6} = 8370$, which is almost doubled (1.93). Because of the fourth/quarter power relationships in Eqns 18 and 19, k decreases by $1.93^{1/4} \approx 18\%$ with L increasing by the same to around $0.093 \times 1.19 b^2/\sqrt{Rt} \approx (1/9) \cdot b^2/\sqrt{Rt}$ for isotropic materials. A more sophisticated analysis brings marginal (but welcome nevertheless) changes in the ploy length.

Finally, we note the outcome of a more recent study of the problem "in reverse": of the persistence of an end-wise transverse curvature applied to an originally flat strip [26]. Curving the end as such allows the floppy strip to remain straight up to where the transverse curvature disappears, causing it to droop beyond if held aloft. The same action can be demonstrated readily using a pizza slice, indeed, it is expeditious for (moderately) elegant eating.

The mechanical essence of the problem is similar to here, invoking an energetic solution of axial stretching and transverse bending but where the change in Gaussian curvature is assumed to be dominated by the twisting curvature χ_{xy} alone. At a given axial position, the transverse curvature is also assumed to be uniform, and calculus of variations produces a quadratic solution for its axial variation rather than an exponential decay.

Repeating their analysis to include our orthotropic parameter, β, we equate the persistence length to our ploy length, and find:

$$L_\mathrm{P} = \frac{1}{\sqrt{70}} \cdot \frac{1}{\beta^{1/4}} \cdot \frac{b^2}{R^{1/2} t^{1/2}} \tag{21}$$

The numerical pre-factor is exact and equal to 0.119: compare this to the value of $1/9 = 0.111$ just found for our three-term Fourier series approach. But this L_P is a *definitive* length at which χ_y is exactly zero—unlike our decaying χ_y.

We can however compare this L_P to our decaying profiles from the FEA; practical measurements are currently in development. We do this by first plotting the transverse curvature variation along the centreline; we superimpose the solutions from Eqn 12 and Eqn 20 for a large number ($n = 51$) of terms according to the value of k obtained from the three-term Fourier series solution. Equation 21 is then plotted as a single

point on the ordinate for comparison.

Eight different tapes are presented in Fig. 8, whose performances are all rather good—in view of decay trends. Even when the modular ratio is excessive, $\beta = 100$, there is a fair comparison; we have not, however, varied the torsional rigidity, which remains isotropic $(1 - \nu)$. The thickness ranges are set about those of metal tapes, and all initial radii are 10 mm. Provided we conserve ratios of R/t if R is changed, the same reasonable fit is seen.

But by far the most influential parameter is b, wrought by changes in cross-sectional angle. For ξ larger than 60°, theoretical decay rates are significantly smaller than those from the FEA. Using a projected width for b instead of arc-length does not improve matters. The underlying long-wave solution assumptions begin to falter.

Of course we must collate more data, in order to establish which combinations of parameters do best. There is also a need to confirm matters experimentally, which is part of on-going research.

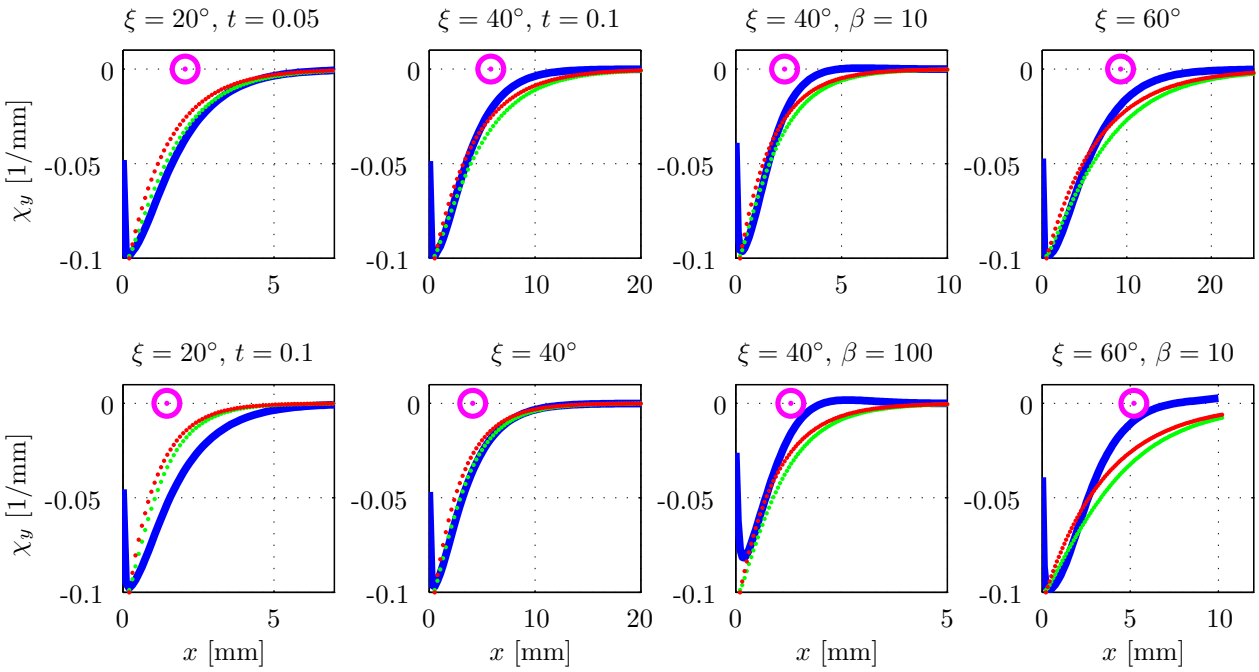

FIGURE 8: Transverse curvature change, χ_y, in ploy regions from FEA (blue) *vs* Eqn 12 (red), and Eqn 20 (green) with $n = 51$, both using k from Eqn 18 with $(B, S) = (0.0674, 8.053 \times 10^{-6})$: purple circles are Eqn 21. All tape-springs have radius 10 mm, thickness 0.2 mm and $\beta = 1$ unless otherwise indicated.

7 Conclusions

We have considered the shape of folded orthotropic tape-springs using finite element analysis, some simple experiments and compact analytical models. The folding process itself is highly non-linear, and differs depending on the direction of bending; there is buckling, either snap-through or torsional, and localisation.

Once folded, the shape is clearly defined: there is an almost developable cylindrical region as the main fold, connected by ploy regions where axial strains and transverse curvature changes are dominant. These properties are consistently observed for isotropic and orthotropic materials, which are demonstrated here for metals and a woven laminated composite. Our study brings together materials and structural mechanics in order to design (provisionally) a multi-functional deployable structure for the aerospace industry.

We have focussed on predicting the radius of the fold, r, and the axial extent of the ploy regions, L_{P}. The former has been shown to depend on the ratio of the Young's moduli, which informs the general trend well, but absolute values of fold radius differ by a few percent when predictions are compared to FEA.

The ploy length complies with a classical long-wave solution in the theory of deformed shells, with a more extensive dependency on the arc-width (b^2), transverse radius ($R^{-1/2}$) and thickness ($t^{-1/2}$): the orthotropic specification enters the pre-factor for L_{P}, which we have determined numerically from energy considerations.

Our study continues with the broader collation of shape data from finite element analysis as well as physical specimens and digital imaging techniques. It is clear that there are shortfalls in our models for different, possibly attractive combinations of geometry and material for alternative composite tape-springs. Rather than exclude these because we cannot predict their folded shapes accurately, we will re-explore our modelling assumptions and devise new insight.

We must also return to the question of how these shapes are affected by the tape-spring being already bistable—which we have excluded here. Finally, we are developing a broader understanding of the structural features, for these govern the ability of the tape to be folded and stowed as part of its landing gear function: given that tapes must also bear compression once deployed and straight, we will be conducting "standard" structural tests of axially loaded, orthotropic thin-walled open tubes.

Acknowledgments: this project is currently funded by Innovate UK under the auspices of *Large Landing Gear of the Future*, in partnership with SAFRAN Landing Systems, grant number RG82506, overall project number 113077 and patent number EP3069991B1 [27]. The insightful comments of two anonymous referees were gratefully received and duly implemented.

References

[1] S D Guest and S Pellegrino, Analytical models for bistable cylindrical shells, *Proceedings of the Royal Society of London, A* (2006) 462, pp. 839-854

[2] A Fernandes and C Maurini and S Vidoli, Multiparameter actuation for shape control of bistable composite plates, *International Journal of Solids and Structures* (2010) 47(10), pp. 1449-1458

[3] L Giomi and L Mahadevan, Multi-stability of free spontaneously curved anisotropic strips, *Proceedings of the Royal Society of London, A* (2012) 468, pp. 511-530

[4] B Budiansky and N A Fleck, Compressive failure of fibre composites, *Journal of the Mechanics and Physics of Solids* (1993) 41(1), pp. 183-211

[5] N A Fleck and P M Jelf and P T Curtis, Compressive failure of laminated and woven composites, *Journal of Composites, Technology and Research* (1995) 17(3), pp. 212-220

[6] C A Steeves and N A Fleck, In-plane properties of composite laminates with through-thickness pin reinforcement, *International journal of Solids and Structures* (2006) 43(10), pp. 3197-3212

[7] B P Russell and K Karthikeyan and V S Deshpande and N A Fleck, The high strain rate response of ultra high molecular-weight polyethylene: from fibre to laminate, *International Journal of Impact Engineering* (2013) 60, pp. 1-9

[8] K Karthikeyan and B P Russell and N A Fleck and H N G Wadley and V S Deshpande, The effect of shear strength on the ballistic response of laminated composite plates, *European Journal of Mechanics-A/Solids* (2013) 42, pp. 35-53

[9] E H Mansfield, Large-deflexion torsion and flexure of initially curved strips, *Proceedings of the Royal Society of London, A* (1973) 334, pp. 279-298

[10] K A Seffen, *Analysis of Structures Deployed by Tape-Springs* (1997) PhD Dissertation, University of Cambridge

[11] B Wang and K A Seffen and S D Guest, Folding of a bistable tape-spring structure based on plain-woven composite, *Proceedings of the 26th Annual Conferece of Composites/Nano Engineering (ICCE-26)* (2018) Paris, France

[12] K A Seffen, 'Morphing' bistable orthotropic elliptical shallow shells, *Proceedings of the Royal Society of London, A* (2007) 463, pp. 67-83

[13] C R Calladine, *Theory of Shell Structures* (1983), Cambridge University Press

[14] K A Seffen and S Pellegrino, Deployment dynamics of tape-springs, *Proceedings of the Royal Society of London, A* (1999) 455, pp. 1003-1048

[15] Hibbitt and Karlsson and Sorensen, *ABAQUS/Standard User's Manual, Version 6.14* (2014)

[16] N K Naik and V K Ganesh, An analytical method for plain weave fabric composites, *Composites* (1995) 26(4), pp. 281-289

[17] K A Seffen, On the behaviour of folded Tape-Springs, *Journal of Applied Mechanics, Transactions ASME* (2000) 68, pp. 369-375

[18] C R Calladine, The theory of thin shell structures 1888-1988: Love Centenary Lecture, *Proceedings of the Insititute of Mechanical Engineers* (1988) 202, pp. 141-149

[19] K Schulgasser, Configuration of a bent tape of curved cross-section, *Journal of Applied Mechanics, Transactions ASME* (1992) 59(3), pp. 692-693

[20] J C H Yee, O Soykasap, S Pellegrino, Carbon Fibre Reinforced Plastic Tape Springs, *Proceedings of the 45th AIAA/ASME/ASCE/AHS/ASC Structures, Structural Dynamics and Materials Conference* (2004) Palm Springs, USA

[21] L Mahadevan and A Vaziri and M Das, Persistence of a pinch in a pipe, *EPL* (2007), paper 40003

[22] A Pocheau and B Roman, Reversibility of crumpling on compressed thin sheets, *European Physical Journal E* (2014) 37, paper 28

[23] M Taffetani and X Jiang and D P Holmes and D Vella, Static bistability of spherical caps, *Proceedings of the Royal Society of London, A* (2018) 474, paper 20170910

[24] V K Jain and F P J Rimrott, The ploy region of a slit tube, *Canadian Aeronautics and Space Institute (CASI) Transactions* (1971) 4(2), pp. 140-144

[25] *MATLAB Release 2013b* (2013) The MathWorks, Inc., Natick, Massachusetts, United States

[26] T Barois and L Tadrist and C Quilliet and Y Forterre, How a curved elastic strip opens, *Physical Review Letters* (2014) 113, paper 214301

[27] R K Schmidt, Aircraft landing gear assembly. Patent EP3069991B1, date of publication: 25/10/2017.